Journal of Sound and Vibration (2002) **255**(3), 555–577
doi:10.1006/jsvi.2001.4180, available online at http://www.idealibrary.com on IDEAL®

PHYSICAL AND NUMERICAL MODELLING OF THE DYNAMIC BEHAVIOR OF A FLY LINE

C. GATTI–BONO AND N. C. PERKINS

Department of Mechanical Engineering, University of Michigan, Ann Arbor, MI 48109, *U.S.A.*

(*Received* 6 *July* 2001, *and in final form* 15 *November* 2001)

The planar equations of motion for a tapered fly line subjected to tension, bending, aerodynamic drag, and weight are derived. The resulting theory describes the large non-linear deformation of the line as it forms a propagating loop during fly casting. A cast is initiated by the motion of the tip of the fly rod that represents the boundary condition at one end of the fly line. At the opposite end, the boundary condition describes the equations of motion of a small attached fly (point mass with air drag). An efficient numerical algorithm is reviewed that captures the initiation and propagation of a non-linear wave that describes the loop. The algorithm is composed of three major steps. First, the non-linear initial-boundary-value problem is transformed into a two-point boundary-value problem, using finite differencing in time. The resulting non-linear boundary-value problem is linearized and then transformed into an initial-value problem in space. Example results are provided that illustrate how an overhead cast develops from initial conditions describing a perfectly laid out back cast. The numerical solutions are used to explore the influence of two sample effects in fly casting, namely, the drag created by the attached fly and the shape of the rod tip path.

1. INTRODUCTION

A major goal in the sport of fly fishing is the presentation of an artificial fly to a feeding fish by casting a fly line. Proficient fly casters often learn through considerable practice and by instruction as provided in courses, books and videos on fly casting techniques; see, for example, [1] or [2]. As noted in [2], "Whenever I question my students about what aspect of fly fishing they want to learn, the majority always answer that more than anything else, they want to become good casters. It is a shame that only a relatively small percentage of anglers will eventually become first-rate casters." While fly casting instruction and techniques vary, they often stress the importance of understanding basic mechanics of the fly line and the fly rod during casting.

Consider a standard overhead cast as illustrated in Figure 1. These idealized sketches illustrate four stages of the forward cast portion of an overhead cast that starts with the fly line laid out horizontally behind the caster at the conclusion of a *back cast*; see Figure 1(a). The caster then rotates the fly rod clockwise, accelerates the fly line, and then abruptly stops the rod as illustrated in Figure 1(b). From this point onwards, the end of the fly line attached to the rod tip remains stationary and a loop necessarily forms between the moving (upper) portion of the fly line and the stationary (lower) portion of the fly line; see Figure 1(b). From the perspective of dynamics, this loop represents a non-linear wave that propagates forward as shown in Figure 1(c) until it reaches the end of the fly line where the loop turns over. This final turnover occurs on or near the surface of the water and the cast is complete.

0022-460X/02/$35.00

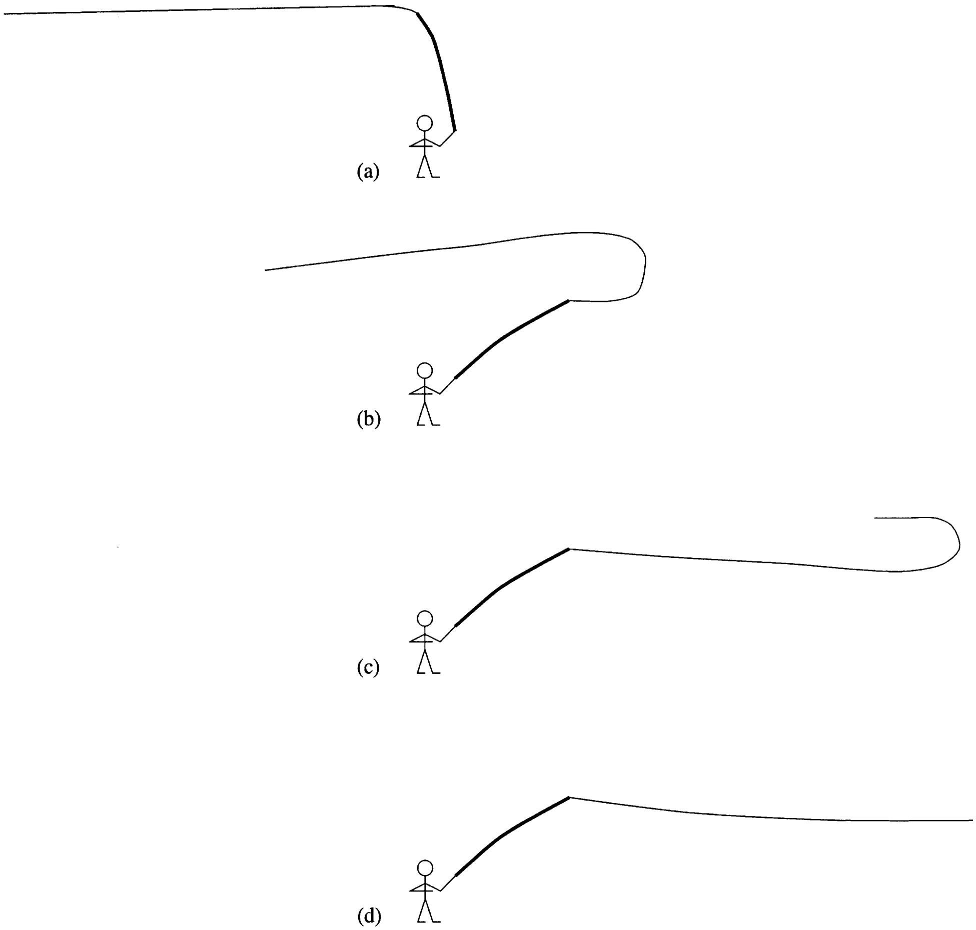

Figure 1. The forward cast of an overhead cast: (a) perfectly laid out back cast; (b) just after stop of forward cast; (c) loop propagation; (d) completion of cast (loop turnover).

The equipment required to achieve such a cast has evolved through years of meticulous experimentation and designs have profited greatly from new materials introduced from other industries [3]. To date, however, the fly fishing industry has not fully exploited the use of computer-based simulation for the design of fly rods and fly lines, or for evaluating fly casting techniques and instruction methods. The opportunity for doing so is recognized, for example, by Phillips [3] who sees a "few innovations that could be on the horizon" that may include "mathematical models of various types of casting strokes, capable of producing casting simulations with specific fly rod designs" and "simulation of flycasting, showing how changes in rod design affect the geometry of the cast" (among the other innovations that he lists). The major goal of this paper is to foster innovations such as these that may result from the computer-based simulation of fly casting.

A limited amount of published research is available on the mechanics of fly casting and much of this is referenced on a website by Spolek [4]. Among the technical papers referenced therein, three studies [5–7] are most closely related to this work as they present models for fly line dynamics. Spolek [5] introduces an idealized model of the fly line for an overhead cast by prescribing *a priori* the geometry of the line. The line is subdivided into three segments consisting of two straight and horizontal segments for the upper and lower portions of the loop and one semi-circular segment for the front of the loop (as might be suggested by the sketch in Figure 1(c)). A work–energy balance is used to study the propagation of this ideal "semi-circular loop" and the key effects caused by tapering† the fly line and by air drag are studied. A refined drag model is subsequently offered in [6] for essentially the same fly line model. In [7], Robson relaxes assumptions in [5, 6] for an ideal semi-circular loop by introducing a multi-body approximation of the continuous fly line. The fly line is modelled as a long chain of particles connected by small massless and rigid rods. The rods are pinned connected and relative joint angles are introduced as the model degrees of freedom. This approach leads to a large-degree-of-freedom lumped parameter model that can be integrated upon prescribing the motion of the tip of the fly rod. Example simulations illustrate good qualitative agreement for the geometry and propagation of a loop when compared to video images of an overhead cast.

The lumped parameter model in [7] requires the analyst to select the number and length of each "rod" as well as the mass of each lumped "mass". These parameters are not known from the description of the fly line and they can also be chosen in a multitude of ways leading to *ad hoc* formulations. Moreover, the model does not account for the bending stiffness of the fly line, although bending stiffness will play an increasingly greater role when the tension in the fly line approaches zero (and in regions of compression). Note that the "stop" of the rod in the forward cast produces a rapid deceleration of the rod tip, which is likely to lead to a significant reduction in the tension of the fly line in this region. In addition, the tension at the end of the fly line is expected to be rather small during the loop turnover. Therefore, models of fly line that lack bending rigidity may be unable to resolve the mechanics in the critical low-tension regions associated with loop formation and loop turnover.

A natural alternative to a lumped parameter model of a fly line is a continuum model that draws from the literature on cable dynamics [8]. The distributed mass and the taper of a fly line can be readily incorporated in a continuum model using available fly line design data (e.g., taper tables). In doing so, one must again recognize the key role played by bending stiffness in regions where the tension approaches zero or is negative (compression). This point is discussed in [9] where it is shown that a model of a perfectly flexible cable becomes ill-posed whenever the tension approaches zero (or is negative). The addition of bending stiffness (or other terms with higher order spatial derivatives) renders the problem well-posed. Models and numerical algorithms have been developed for fluid-loaded cables (with bending) using finite differencing methods as motivated by ocean engineering applications; see, for example, [10–12]. Of these, we will adapt and modify the strategy in [12] for simulating the dynamics of fly casting. The main advantage of this strategy is that the solution scheme, unlike box methods, does not involve a shooting method, which we found to be difficult to use for our application.

The objective of this paper is to establish a new continuum model for fly line dynamics and to describe a numerical algorithm for simulating flycasting. The model, which is presented in section 2, accounts for the principal forces affecting fly line dynamics including fly line tension, drag, self-weight, shear and related bending. This model takes the form of a very long and non-uniform (tapered) elastica that captures the non-linear dynamic deformations responsible for loop formation and propagation. The numerical algorithm is detailed in section 3 and results for overhead casts are reviewed in section 4. Example simulations are used to explore the influence of two sample effects in casting; namely, the drag created by the attached fly, and the shape of path described by the rod tip.

---

†The term *taper* refers to the intentional changes in the cross-sectional area of the fly line that significantly influences casting. An example is provided in section 4.

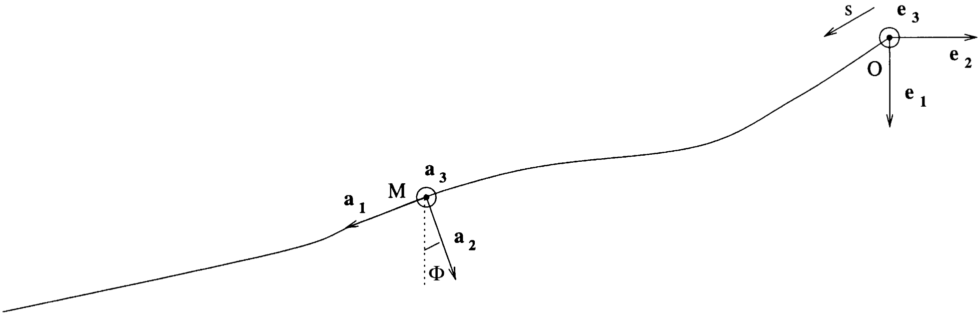

Figure 2. Definition of the inertial reference frame ($\mathbf{e}_1, \mathbf{e}_2, \mathbf{e}_3$) and the local (Serret–Frénet) reference frame ($\mathbf{a}_1, \mathbf{a}_2, \mathbf{a}_3$). The Lagrangian coordinate s measures the arc length along the line.

2. CONTINUUM MODEL

In this section, we derive the two-dimensional equations of motion for a fly line subject to tension, bending, aerodynamic drag and weight. The mechanical model is that of a long and non-uniform elastica with very small bending stiffness similar to that used by Sun [12] to model low-tension underwater cables. We begin by first introducing two reference frames that are convenient for formulating the theory. We then derive the compatibility equation, the linear and angular momentum equations, and the constitutive equation that define the fly line model. Finally, we will specify the initial conditions and the boundary conditions for the forward cast of a standard overhead cast.

2.1. FRAMES OF REFERENCE

Figure 2 illustrates two reference frames employed in the following derivation. The inertial reference frame ($O, \mathbf{e}_1, \mathbf{e}_2, \mathbf{e}_3$) is fixed in space and is the natural choice for describing the acceleration components and weight of the fly line. The Serret–Frénet reference frame (M, $\mathbf{a}_1$, $\mathbf{a}_2$, $\mathbf{a}_3$) is a local reference frame attached to the fly line at any point M and is the natural choice for describing the tension, bending and aerodynamic drag of the line. Here, $\mathbf{a}_1$ is the unit tangent vector, $\mathbf{a}_2$ is the unit normal vector, and $\mathbf{a}_3$ is the unit bi-normal vector. The following transformation between the two reference frames is a function of the Euler angle Φ shown in Figure 2. Let (z_1, z_2) be the components of a vector $\mathbf{z}$ in the local reference frame and let (Z_1, Z_2) be the components of $\mathbf{z}$ in the inertial reference frame. These components are related through

$$\begin{Bmatrix} z_1 \\ z_2 \end{Bmatrix} = \mathbf{L} \begin{Bmatrix} Z_1 \\ Z_2 \end{Bmatrix} = \begin{bmatrix} \sin\Phi & -\cos\Phi \\ \cos\Phi & \sin\Phi \end{bmatrix} \begin{Bmatrix} Z_1 \\ Z_2 \end{Bmatrix}, \tag{1}$$

where $\mathbf{L}$ is the associated rotation matrix.

2.2. COMPATIBILITY EQUATION

In developing the equations of motion, we must evaluate derivatives with respect to both space and time. The spatial derivatives are taken with respect to a Lagrangian coordinate s that defines the arc length along the line as shown in Figure 2. Derivatives will be formed with respect to both the local and inertial reference frames as follows. Let $\mathbf{z}$ be an arbitrary vector with the following representation in the local reference frame:

$$\mathbf{z} = z_1\mathbf{a}_1 + z_2\mathbf{a}_2. \tag{2}$$

Let $\mathrm{D}\mathbf{z}/\mathrm{D}t$ be the derivative of $\mathbf{z}$ with respect to time as seen by an observer in the inertial reference frame. Then [13]

$$\frac{\mathrm{D}\mathbf{z}}{\mathrm{D}t} = \left(\frac{\mathrm{d}\mathbf{z}}{\mathrm{d}t}\right)_{(\mathbf{a}_1,\mathbf{a}_2,\mathbf{a}_3)} + \boldsymbol{\omega} \times \mathbf{z}, \tag{3}$$

where $(\mathrm{d}\mathbf{z}/\mathrm{d}t)_{(\mathbf{a}_1,\mathbf{a}_2,\mathbf{a}_3)}$ is the derivative of the vector $\mathbf{z}$ with respect to time as seen by an observer in the local reference frame and $\boldsymbol{\omega}$ is the angular velocity of the local frame of reference

$$\boldsymbol{\omega} = \frac{\partial \Phi}{\partial t}\mathbf{e}_3. \tag{4}$$

Similarly, the derivative of $\mathbf{z}$ with respect to the spatial coordinate s as seen by an observer in the inertial reference frame is

$$\frac{\mathrm{D}\mathbf{z}}{\mathrm{D}s} = \left(\frac{\mathrm{d}\mathbf{z}}{\mathrm{d}s}\right)_{(\mathbf{a}_1,\mathbf{a}_2,\mathbf{a}_3)} + \boldsymbol{\kappa} \times \mathbf{z}, \tag{5}$$

where $(\mathrm{d}\mathbf{z}/\mathrm{d}s)_{(\mathbf{a}_1,\mathbf{a}_2,\mathbf{a}_3)}$ is the derivative of the vector $\mathbf{z}$ with respect to s as seen by an observer in the local reference frame and $\boldsymbol{\kappa}$ is the curvature vector of the planar curve formed by the line given by

$$\boldsymbol{\kappa} = \frac{\partial \Phi}{\partial s}\mathbf{e}_3. \tag{6}$$

The above results will now be employed in deriving the kinematical quantities required for formulating the equations of motion. We begin by noting that the unit tangent vector is given by

$$\mathbf{a}_1 = \frac{\partial \mathbf{r}}{\partial s}, \tag{7}$$

where $\mathbf{r}$ denotes the position of a material point of the line.

The unit normal vector is then given by

$$\mathbf{a}_2 = \frac{1}{|\kappa|}\frac{\partial \mathbf{a}_1}{\partial s}. \tag{8}$$

The velocity vector of a material point is

$$\mathbf{v} = \frac{\mathrm{D}\mathbf{r}}{\mathrm{D}t} \tag{9}$$

and the velocity gradient is then

$$\frac{\mathrm{D}\mathbf{v}}{\mathrm{D}s} = \frac{\mathrm{D}}{\mathrm{D}s}\left(\frac{\mathrm{D}\mathbf{r}}{\mathrm{D}t}\right). \tag{10}$$

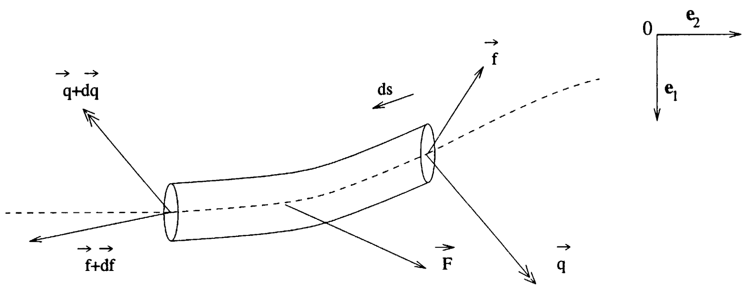

Figure 3. Definition of the forces and moments acting on the fly line.

Recognize that the position vector **r** is a vector-valued function of class $\mathscr{C}^2$. Therefore, the order of differentiation in equation (10) can be interchanged:

$$\frac{\mathrm{D}\mathbf{v}}{\mathrm{D}s}=\frac{\mathrm{D}}{\mathrm{D}t}\left(\frac{\mathrm{D}\mathbf{r}}{\mathrm{D}s}\right). \tag{11}$$

Equating equations (10) and (11) and employing equations (3), (5), and (7) leads to the compatibility equation

$$\frac{\partial\mathbf{v}}{\partial s}+\boldsymbol{\kappa}\times\mathbf{v}=\boldsymbol{\omega}\times\mathbf{a}_1 \tag{12}$$

that relates the above kinematical quantities.

2.3. LINEAR AND ANGULAR MOMENTUM EQUATIONS

The momentum equations for an infinitesimal element of the fly line depicted in Figure 3 will now be summarized. Linear and angular momentum balances of this infinitesimal element result in

$$\frac{\mathrm{D}\mathbf{f}}{\mathrm{D}s}+\mathbf{F}=\rho_l A(s)\frac{\mathrm{D}\mathbf{v}}{\mathrm{D}t}, \tag{13}$$

$$\frac{\mathrm{D}\mathbf{q}}{\mathrm{D}s}+\mathbf{a}_1\times\mathbf{f}=\frac{\mathrm{D}\mathbf{H}}{\mathrm{D}t}, \tag{14}$$

where it is assumed that no external distributed moments act. Here, $\mathbf{f}=f_1\mathbf{a}_1+f_2\mathbf{a}_2$ is the internal force with tension (f_1) and shear (f_2) components, $\mathbf{F}=F_1\mathbf{a}_1+F_2\mathbf{a}_2$ is the external force per unit length, ρ_l is the fly line density, $A(s)$ is the (spatially varying) line cross-section, $\mathbf{q}=q_3\mathbf{e}_3$ is the internal moment, and $\mathbf{H}=H_3\mathbf{e}_3$ is the angular momentum per unit length. The latter quantity is given by

$$\mathbf{H}=I(s)\boldsymbol{\omega}, \tag{15}$$

where

$$I(s)=\frac{\rho_l\pi D^4(s)}{64} \tag{16}$$

for the line of circular cross-section with (spatially varying) diameter $D(s)$.

Expanding equations (13) and (14) using equations (3) and (5) results in

$$\frac{\partial \mathbf{f}}{\partial s} + \boldsymbol{\kappa} \times \mathbf{f} + \mathbf{F} = \rho_l A(s)\left(\frac{\partial \mathbf{v}}{\partial t} + \boldsymbol{\omega} \times \mathbf{v}\right), \tag{17}$$

$$\frac{\partial q_3}{\partial s} + f_2 = \frac{\partial H_3}{\partial t}. \tag{18}$$

2.4. CONSTITUTIVE EQUATION

We now introduce a linear constitutive law for line bending,

$$q_3 = EJ(s)\kappa, \tag{19}$$

by employing Kirchhoff assumptions for a slender rod. Here, E denotes Young's modulus for the fly line and

$$J(s) = \frac{I(s)}{\rho_l}. \tag{20}$$

2.5. SUMMARY OF FLY LINE MODEL

Equations (6), (12), and (17)–(19) yield a system of seven scalar equations containing seven unknowns $f_1, f_2, q_3, v_1, v_2, \kappa$, and Φ. Substituting equation (19) into equation (18) reduces these to the following set of six equations:

$$\frac{\partial v_1}{\partial s} = \kappa v_2, \quad \frac{\partial v_2}{\partial s} = -\kappa v_1 + \frac{\partial \Phi}{\partial t}, \quad \frac{\partial \Phi}{\partial s} = \kappa, \tag{21–23}$$

$$\frac{\partial \kappa}{\partial s} = \frac{1}{EJ}\left(-f_2 - \frac{\pi E D^3}{16}\kappa + \frac{\partial (I \frac{\partial \Phi}{\partial t})}{\partial t}\right), \tag{24}$$

$$\frac{\partial f_1}{\partial s} = \kappa f_2 - F_1 + \rho_l A(s)\left(\frac{\partial v_1}{\partial t} - \frac{\partial \Phi}{\partial t} v_2\right), \tag{25}$$

$$\frac{\partial f_2}{\partial s} = -\kappa f_1 - F_2 + \rho_l A(s)\left(\frac{\partial v_2}{\partial t} + \frac{\partial \Phi}{\partial t} v_1\right) \tag{26}$$

in the six unknowns $(v_1, v_2, \Phi, \kappa, f_1, f_2)$.

The first three equations (21), (22), and (23) define an inextensibility constraint, the angular velocity, and the curvature respectively. The remaining three equations (24), (25), and (26) represent the angular and the two linear momentum equations respectively. These momentum equations will now be completed by defining the external forces per unit length F_1 and F_2 acting on the fly line by accounting for aerodynamic drag and self-weight.

A standard (Morison) drag formulation is adopted. Let C_{d1} and C_{d2} denote drag coefficients associated with tangential drag (skin friction) and normal drag respectively. Then, the drag per unit length

$$\mathbf{h} = h_1 \mathbf{a}_1 + h_2 \mathbf{a}_2 \tag{27}$$

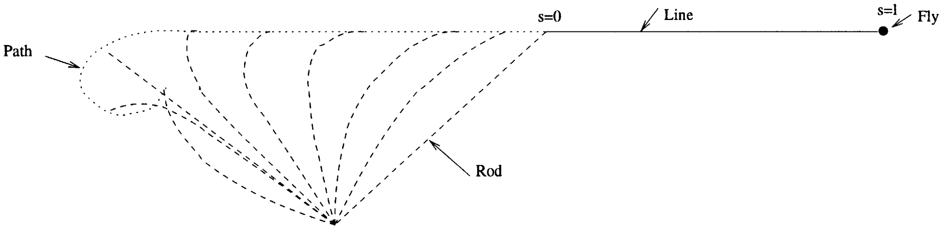

Figure 4. Initial and boundary conditions for an overhead cast. Initial conditions describe the fly line at rest in a perfect back cast (solid curve). The boundary condition at $s = 0$ defines the prescribed motion of the rod tip. The boundary condition at $s = l$ defines the equations of motion of the attached fly.

has components

$$h_1 = -\tfrac{1}{2}\rho_a D(s)\pi C_{d1} v_1 |v_1|, \quad h_2 = -\tfrac{1}{2}\rho_a D(s) C_{d2} v_2 |v_2|, \qquad (28, 29)$$

where ρ_a is the density of air. Adding now the tangential and normal components of the weight of the fly line per unit length provides

$$F_1 = h_1 + \rho_l g A(s)\sin(\Phi), \quad F_2 = h_2 + \rho_l g A(s)\cos(\Phi). \qquad (30, 31)$$

2.6. INITIAL AND BOUNDARY CONDITIONS

The definition of the fly line model is now completed by adding the initial and the boundary conditions. The forward cast of an overhead cast is modelled starting at rest from a perfectly laid out back cast as shown in Figure 4. Hence, the initial conditions are

$$v_1(s, 0) = 0, \quad v_2(s, 0) = 0, \quad \Phi(s, 0) = \pi, \quad \frac{\partial \Phi}{\partial t}(s, 0) = 0. \qquad (32\text{–}35)$$

From these initial conditions, the rod tip is accelerated to the left through the forward stroke of the overhead cast as illustrated in Figure 4. The velocity of the rod tip defines the boundary conditions at this end of the fly line ($s = 0$). The shape of the rod tip path and the velocity along this path must be known *a priori* to provide boundary conditions to the fly line model studied in this paper. They are estimated from video footage [16] for a typical cast (i.e., for the coupled system composed of the fly line and the fly rod). Thus, while the fly rod is not modelled herein, its influence (including its flexibility) is captured in this *measured* boundary condition. As depicted in Figure 4, the path of the tip of the fly rod is nominally straight and horizontal due to the considerable bending of the fly rod as it accelerates the fly line. The rod is then abruptly decelerated to a stop and the rod unloads in the fundamental bending mode creating additional rod tip/fly line speed. During this unloading, the rod tip path is likely to dip downwards slightly and this effect is exaggerated in Figure 4. Thus, the boundary conditions at this end are

$$v_1(0, t) = g_1(t), \quad v_2(0, t) = g_2(t), \quad \kappa(0, t) = 0, \qquad (36\text{–}38)$$

where $g_1(t)$ and $g_2(t)$ are the assumed-known velocity components of the rod tip and where a hinged connection to the fly rod is assumed. The boundary conditions at the opposite end ($s = l$) describe the equations of motion of the attached fly. We model the fly as a particle

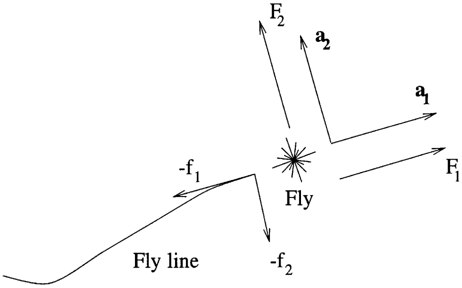

Figure 5. Free-body diagram of the fly. $\mathbf{F} = F_1\mathbf{a}_1 + F_2\mathbf{a}_2$ includes the fly weight and air drag. $\mathbf{f} = f_1\mathbf{a}_1 + f_2\mathbf{a}_2$ includes the tension and shear reactions from the attached fly line.

subject to tension from the fly line, self-weight, and air drag. Linear and angular momentum balances for the fly, depicted as a free body in Figure 5, lead to

$$m_f\left(\frac{\partial v_1}{\partial t}(l,t) - \frac{\partial \Phi}{\partial t}(l,t)v_2(l,t)\right) = m_f g\sin(\Phi(l,t)) - \beta_f\sqrt{v_1^2(l,t)+v_2^2(l,t)}\,v_1(l,t) - f_1(l,t), \tag{39}$$

$$m_f\left(\frac{\partial v_2}{\partial t}(l,t) + \frac{\partial \Phi}{\partial t}(l,t)v_1(l,t)\right) = m_f g\cos(\Phi(l,t)) - \beta_f\sqrt{v_1^2(l,t)+v_2^2(l,t)}\,v_2(l,t) - f_2(l,t), \tag{40}$$

$$\kappa(l,t) = 0. \tag{41}$$

Here, m_f is the mass of the fly, and $\beta_f = \frac{1}{2}\rho_a A_f C_{df}$ in which A_f is the projected area of the fly, and C_{df} is the drag coefficient for the fly.

3. NUMERICAL ALGORITHM

The non-linear initial-boundary-value problem above is solved using space–time finite differencing. The algorithm is a modification of that developed in references [12, 14]. The key steps in the algorithm are as follows.

- Transform the space–time problem (21)–(26) into a spatial two-point boundary-value problem using finite differencing in time.
- Approximate the resulting non-linear differential equations as a system of linear differential equations using a first order Taylor series expansion to obtain a linear two-point boundary-value problem.
- Transform the linear two-point boundary-value problem into a linear initial-value problem which can then be solved efficiently and then iterate for non-linear corrections by updating the Taylor series expansion above.

These steps are detailed below.

System (21)–(26) can be rewritten as

$$\frac{\partial \mathbf{y}}{\partial s} = \mathscr{F}\left(\mathbf{y}(s,t), \frac{\partial \mathbf{y}}{\partial t}(s,t), \frac{\partial^2 \mathbf{y}}{\partial t^2}(s,t)\right), \tag{42}$$

$$\mathbf{h}_o\left(\mathbf{y}(0,t),\frac{\partial \mathbf{y}}{\partial t}(0,t)\right)=0,\qquad \mathbf{h}_L\left(\mathbf{y}(l,t),\frac{\partial \mathbf{y}}{\partial t}(l,t)\right)=0, \tag{43, 44}$$

where $\mathbf{h}_o$ (respectively $\mathbf{h}_L$) represents the three boundary conditions (36)–(38) (respectively equations (39)–(41)) and $\mathbf{y}(s,t)$ is the vector of unknowns

$$\mathbf{y}(s,t)=[v_1 \quad v_2 \quad \Phi \quad \kappa \quad f_1 \quad f_2]^{\mathrm{T}}. \tag{45}$$

Expressing $(\partial\mathbf{y}/\partial t)(s,t)$ and $(\partial^2\mathbf{y}/\partial t^2)(s,t)$ in terms of known or guessed quantities at the previous time step $(\hat{t}-\Delta t)$ and current time step $\hat{t}$ using finite differencing removes the time dependence and yields a discrete non-linear two-point boundary-value problem at each time step. The time discretization employed is a stable, implicit integration scheme using a Newmark-like method. The time derivative of a scalar quantity z is approximated by

$$\frac{\partial z}{\partial t}(s,\hat{t})=\frac{z(s,\hat{t})-z(s,\hat{t}-\Delta t)}{\alpha\Delta t}-\gamma\frac{\partial z}{\partial t}(s,\hat{t}-\Delta t) \tag{46}$$

in which α and γ are integration parameters that are related by

$$\gamma=\frac{(1-\alpha)}{\alpha}. \tag{47}$$

Note that the choice $\alpha = 1$ and $\gamma = 0$ reduces equation (46) to backwards differencing. In reference [14], Sun showed that numerical damping is introduced when using a backward difference scheme and that numerical damping is removed by choosing $\alpha = 0{\cdot}5$. In this study, we will use $\alpha = 0{\cdot}6$ because adding small numerical damping aids numerical convergence but also remains quite small relative to the physical damping associated with air drag.

The finite differencing strategy for the acceleration vector is different from the one employed by Sun in [12]. Indeed, the strategy in [12] is limited to small rotations and accelerations of the local reference frame. In fly casting, the rotations and accelerations are large enough that Sun's method leads to a 200% error in the acceleration when the acceleration peak is reached in the forward cast. Herein, discretization (46) is applied to the components of the acceleration vector in the inertial reference frame. Using equation (1) and the fact that the transformation matrix $\mathbf{L}$ is orthogonal, the velocity components $(\dot{X}_1, \dot{X}_2)$ in the inertial reference frame are related to those (v_1, v_2) in the local reference frame through

$$\begin{Bmatrix}\dot{X}_1\\ \dot{X}_2\end{Bmatrix}=\mathbf{L}^{\mathrm{T}}\begin{Bmatrix}v_1\\ v_2\end{Bmatrix}. \tag{48}$$

Taking the time derivative of equation (48) and using the fact that the $\mathbf{L}$ is orthogonal yields

$$\begin{Bmatrix}\dfrac{\partial v_1}{\partial t}(s,\hat{t})\\[2ex] \dfrac{\partial v_2}{\partial t}(s,\hat{t})\end{Bmatrix}=\mathbf{L}\begin{Bmatrix}\dfrac{\dot{X}_1(s,\hat{t})-\dot{X}_1(s,\hat{t}-\Delta t)}{\alpha\Delta t}-\gamma\ddot{X}_1(s,\hat{t}-\Delta t)\\[2ex] \dfrac{\dot{X}_2(s,\hat{t})-\dot{X}_2(s,\hat{t}-\Delta t)}{\alpha\Delta t}-\gamma\ddot{X}_2(s,\hat{t}-\Delta t)\end{Bmatrix}-\mathbf{L}\frac{\partial\mathbf{L}^{\mathrm{T}}}{\partial\mathbf{t}}\begin{Bmatrix}v_1(s,\hat{t})\\ v_2(s,\hat{t})\end{Bmatrix}. \tag{49}$$

Using the time discretization above, equations (42)–(44) can be rewritten in the following forms:

$$\frac{\mathrm{d}\mathbf{y}}{\mathrm{d}s}(s, \hat{t}) = \mathscr{F}(\mathbf{y}(s, \hat{t} - \Delta t), \mathbf{y}(s, \hat{t})), \tag{50}$$

$$\mathbf{h}_o(\mathbf{y}(0, \hat{t})) = 0, \qquad \mathbf{h}_L(\mathbf{y}(l, \hat{t})) = 0, \tag{51, 52}$$

resulting in a non-linear two-point boundary-value problem.

Let $\mathbf{y}$ be the exact solution of equations (50)–(52) and $\mathbf{y}^*$ be an approximate solution. Equations (50)–(52) can be expanded in a first order Taylor series about the approximate solution $\mathbf{y}^*$ as follows:

$$\frac{\mathrm{d}\mathbf{y}}{\mathrm{d}s}(s, \hat{t}) = \mathscr{F}(\mathbf{y}^*(s, \hat{t})) + \left[\frac{\partial \mathscr{F}}{\partial \mathbf{y}}\right]_{\mathbf{y}^*(s,\hat{t})} (\mathbf{y}(s, \hat{t}) - \mathbf{y}^*(s, \hat{t})), \tag{53}$$

$$\mathbf{h}_o(\mathbf{y}^*(0, \hat{t})) + \left[\frac{\partial \mathbf{h}_o}{\partial \mathbf{y}}\right]_{\mathbf{y}^*(0,\hat{t})} (\mathbf{y}(0, \hat{t}) - \mathbf{y}^*(0, \hat{t})) = 0, \tag{54}$$

$$\mathbf{h}_L(\mathbf{y}^*(l, \hat{t})) + \left[\frac{\partial \mathbf{h}_L}{\partial \mathbf{y}}\right]_{\mathbf{y}^*(l,\hat{t})} (\mathbf{y}(l, \hat{t}) - \mathbf{y}^*(l, \hat{t})) = 0. \tag{55}$$

Here, $[\partial \mathscr{F}/\partial \mathbf{y}]_{\mathbf{y}^*(s,\hat{t})}$ denotes the 6×6 Jacobian of system (50) evaluated at the approximate solution $\mathbf{y}^*(s, \hat{t})$, $[\partial \mathbf{h}_o/\partial \mathbf{y}]_{\mathbf{y}^*(0,\hat{t})}$ is the 3×6 matrix having components $(\partial (h_o)_i/\partial y_j)$ evaluated at $\mathbf{y}^*(0, \hat{t})$, and $[\partial \mathbf{h}_L/\partial \mathbf{y}]_{\mathbf{y}^*(l,\hat{t})}$ is the 3×6 matrix having components $(\partial (h_L)_i/\partial y_j)$ evaluated at $\mathbf{y}^*(l, \hat{t})$.

Equations (53)–(55) are rewritten as

$$\frac{\mathrm{d}\mathbf{y}}{\mathrm{d}s}(s, \hat{t}) = \mathbf{A}^*(s, \hat{t})\mathbf{y}(s, \hat{t}) + \mathbf{B}^*(s, \hat{t}), \tag{56}$$

$$\mathbf{C}_o^*(t)\mathbf{y}(0, \hat{t}) + \mathbf{D}_o^*(\hat{t}) = 0, \quad \mathbf{C}_L^*(t)\mathbf{y}(l, \hat{t}) + \mathbf{D}_L^*(\hat{t}) = 0, \tag{57, 58}$$

where

$$\mathbf{A}^*(s, \hat{t}) = \left[\frac{\partial \mathscr{F}}{\partial \mathbf{y}}\right]_{\mathbf{y}^*(s,\hat{t})}, \quad \mathbf{B}^*(s, \hat{t}) = \mathscr{F}(\mathbf{y}^*(s, \hat{t})) - \left[\frac{\partial \mathscr{F}}{\partial \mathbf{y}}\right]_{\mathbf{y}^*(s,\hat{t})} \mathbf{y}^*(s, \hat{t}),$$

$$\mathbf{C}_o^*(\hat{t}) = \left[\frac{\partial \mathbf{h}_o}{\partial \mathbf{y}}\right]_{\mathbf{y}^*(0,\hat{t})}, \quad \mathbf{D}_o^*(\hat{t}) = \mathbf{h}_o(\mathbf{y}^*(0, \hat{t})) - \left[\frac{\partial \mathbf{h}_o}{\partial \mathbf{y}}\right]_{\mathbf{y}^*(0,\hat{t})} \mathbf{y}^*(0, \hat{t}),$$

$$\mathbf{C}_L^*(\hat{t}) = \left[\frac{\partial \mathbf{h}_L}{\partial \mathbf{y}}\right]_{\mathbf{y}^*(l,\hat{t})}, \quad \mathbf{D}_L^*(\hat{t}) = \mathbf{h}_L(\mathbf{y}^*(l, \hat{t})) - \left[\frac{\partial \mathbf{h}_L}{\partial \mathbf{y}}\right]_{\mathbf{y}^*(l,\hat{t})} \mathbf{y}^*(l, \hat{t}).$$

The system (56)–(58) defines a two-point linear boundary-value problem for solution of $\mathbf{y}(s, \hat{t})$ in an affine space of dimension 6. A solution of the form

$$\mathbf{y}(s, \hat{t}) = \mathbf{y}_p(s, \hat{t}) + \mathbf{y}_h(s, \hat{t})\boldsymbol{\xi} \tag{59}$$

is sought where $\mathbf{y}_p(s, \hat{t})$ is a particular solution and $\mathbf{y}_h(s, \hat{t})$ is a homogeneous solution. The 3×1 vector $\boldsymbol{\xi}$ in equation (59) contains the unknown constants of integration that will be determined using the terminal end ($s = l$) boundary conditions. These solution components satisfy the linear initial-value problems below.

The particular solution is a 6×1 vector that satisfies

$$\frac{\mathrm{d}\mathbf{y}_p}{\mathrm{d}s}(s, \hat{t}) = \mathbf{A}^*(s, \hat{t})\mathbf{y}_p(s, \hat{t}) + \mathbf{B}^*(s, \hat{t}), \tag{60}$$

$$\mathbf{y}_p(0, \hat{t}) = [g_1(\hat{t})g_2(\hat{t}) \;\; 0 \;\; 0 \;\; 0 \;\; 0]^{\mathrm{T}}. \tag{61}$$

The homogeneous solution $\mathbf{y}_h(s, t)$ is a 6×3 matrix that satisfies

$$\frac{\mathrm{d}\mathbf{y}_h}{\mathrm{d}s}(s, \hat{t}) = \mathbf{A}^*(s, \hat{t})\mathbf{y}_h(s, \hat{t}), \quad \mathbf{y}_h(0, \hat{t}) = \begin{bmatrix} 0 & 0 & 1 & 0 & 0 & 0 \\ 0 & 0 & 0 & 0 & 1 & 0 \\ 0 & 0 & 0 & 0 & 0 & 1 \end{bmatrix}^{\mathrm{T}}. \tag{62, 63}$$

Note that the boundary conditions at the starting end ($s = 0$) are always satisfied, regardless of the choice of $\boldsymbol{\xi}$.

The two initial-value problems defined by equations (60)–(63) are integrated separately. The unknown vector $\boldsymbol{\xi}$ is chosen so that the solution vector $\mathbf{y}(s, \hat{t})$ satisfies the terminal end boundary conditions

$$\mathbf{C}_L^*(\hat{t})(\mathbf{y}_p(l, \hat{t}) + \mathbf{y}_h(l, \hat{t})\boldsymbol{\xi}) + \mathbf{D}_L^*(\hat{t}) = 0. \tag{64}$$

Thus, $\boldsymbol{\xi}$ satisfies

$$\boldsymbol{\xi} = -\,[\mathbf{C}_L^*(\hat{t})\mathbf{y}_h(l, \hat{t})]^{-1}\,(\mathbf{C}_L^*(\hat{t})\mathbf{y}_p(l, \hat{t}) + \mathbf{D}_L^*(\hat{t})). \tag{65}$$

One drawback of the method above is that, since all the values of $y(0, \hat{t})$ are not known *a priori*, particular and homogeneous solution components (of exponential type in space) may rapidly grow leading to unrealistically large solution components prior to reaching the terminal end ($s = l$). A suppression method [12, 14, 15] is now introduced to control the growth of these solution components. The method follows from the fact that the "true" solution is bounded, and that we must guess the unknown values of Φ, f_1, and f_2 at the starting end ($s = 0$).

During the simulation, the expected order of magnitude of the variables is known and can be used to check the solution size at "suppression points". If a variable exceeds its expected range, this signals a poor guess of the unknown values for Φ, f_1, and f_2 at the starting end ($s = 0$). These three variables (Φ, f_1, and f_2) are monitored for suppression as detailed in Appendix A.

We now have a method to integrate the linearized, two-point boundary-value problem (56)–(58) starting from the solution at the previous time step. At the current time step, we iterate on the linearized boundary-value problem by updating the solution using this problem from the previous iterate. The iterations stop when the relative difference between

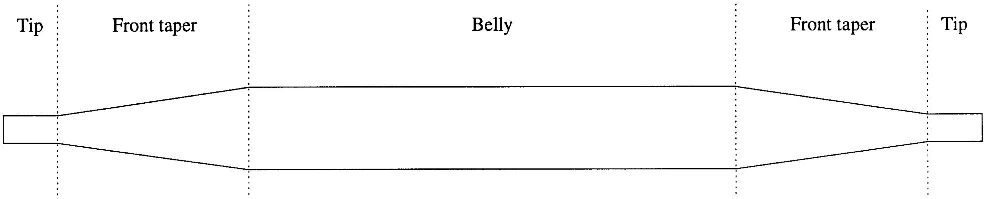

Figure 6. Schematic of the example double-tapered fly line.

TABLE 1

Taper table for line DT-5-F

Section name	Tip	Front taper	Belly	Front taper	Tip
Length of the section (m)	0·152	1·78	23·88	1·78	0·152
Diameter of the section (m)	$0{\cdot}889\times10^{-3}$	—	$1{\cdot}041\times10^{-3}$	—	$0{\cdot}889\times10^{-3}$

TABLE 2

Data for fly casting example

Parameter	Symbol	Value	Units
Bending stiffness	E	$1{\cdot}0\times10^{10}$	N/m^2
Length of the fly line	l	5	m
Density of the fly line	ρ_l	$1{\cdot}158\times10^{3}$	kg/m^3
Gravitational constant	g	9·81	m/s^2
Density of air	ρ_a	1·29	kg/m^3
Tangential drag coefficient of the fly line	C_{d1}	1	
Normal drag coefficient of the fly line	C_{d2}	0·01	
Coarse time step	Δt_1	0·0075	s
Fine time step	Δt_2	0·0002	s
Spatial step	Δs	0·0033	m
Prescribed error	Δe	0·05	
Mass of the fly	m_f	0·000075	kg
Drag coefficient of the fly	C_{df}	1	
Radius of the fly	r_f	0·0075	m

the results of two successive iterations is smaller than a stipulated error tolerance as calculated by

$$\Delta e = \max_{s\in[0,l]}\left(\sqrt{\left(\sum_{i=1}^{6}\left(\frac{\mathbf{y}_i-\mathbf{y}_i^*}{\mathbf{y}_i^*}\right)\right)}\right), \tag{66}$$

where **y** designates the solution from the current iteration and **y*** the solution from the previous iteration. In this manner, an approximate solution to the non-linear boundary-value problem (50)–(52) is found prior to proceeding to the next time step.

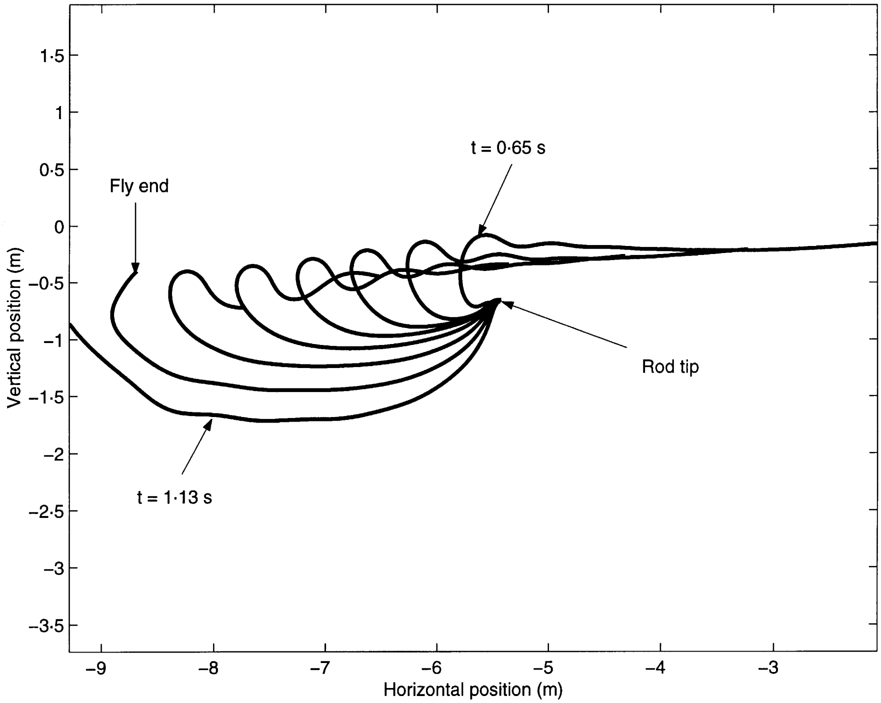

Figure 7. Numerical calculation of a forward cast showing loop formation and loop propagation at eight selected times; $t = 0{\cdot}65$, 0·69, 0·74, 0·80, 0·86, 0·94, 1·03, and 1·13 s.

4. RESULTS

The model and numerical method described above are used to simulate an overhead cast starting from a perfect back cast. An example fly line is selected to be a double-tapered 5 weight floating line (DT-5-F). A schematic of the taper for this line is provided in Figure 6 and the taper information is given in Table 1. The length of the line used in the casts is 5 m and this represents a short cast. The remainder of the parameters chosen for this example are listed in Table 2. Table 2 also includes two parameters, a coarse time step Δt_1 and fine time step Δt_2, that control the integration time stepping. An adaptive time step

$$\Delta t = \Delta t_1 - (\Delta t_1 - \Delta t_2)\left(\frac{\sin(a(t-\tau))}{a(t-\tau)}\right)^4 \tag{67}$$

is used to reduce computational effort as well as to insure numerical stability. Here, a and τ are two parameters that determine the transition from the coarse to the fine time step. Starting from the back cast, the integration begins using the coarse time step and the fly line deforms only modestly as it accelerates along a nearly straight-line path. Near the end of this straight-line acceleration, the rod tip dips slightly below the horizontal as the rod unloads in its fundamental bending mode of vibration. This motion corresponds to a very rapid deceleration of the rod tip (what a fly caster calls a “stop”) that initiates large deformation of the fly line and the formation of a loop. The fine time step is used to resolve this phase of the cast as well as the propagation of the loop thereafter.

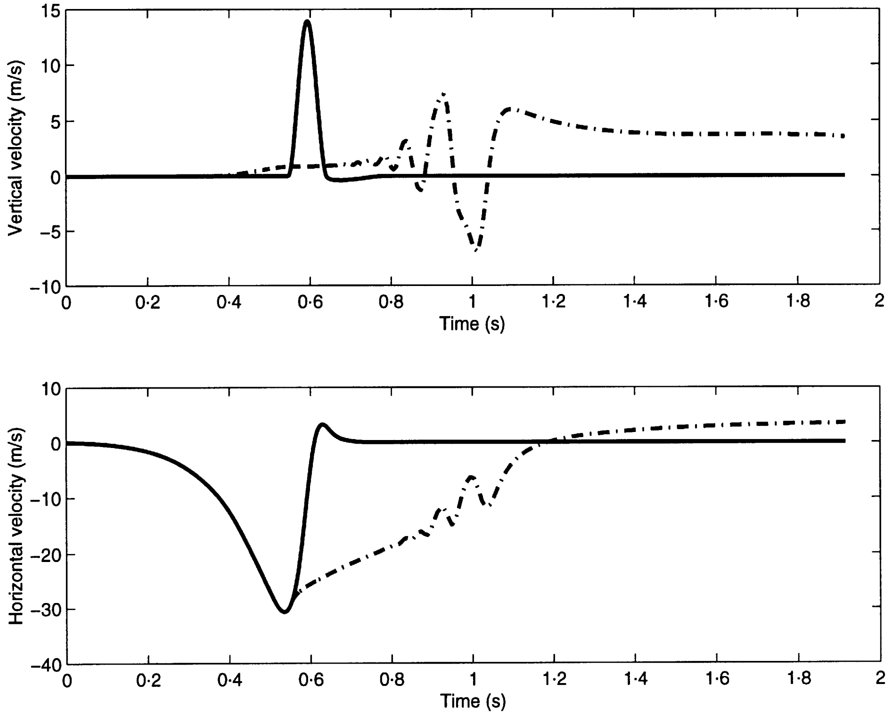

Figure 8. Time history of the velocity components at the extreme ends of the fly line: ——, rod tip end of the fly line; ·–·–·-, fly end of the fly line.

It is also important to note that the initial conditions are smooth (they satisfy the equations of motion) and that the model includes the bending stiffness of the fly line. By contrast, the initial conditions proposed in [4–6] have discontinuities in the fly line curvature (bending was not considered) and these would necessarily generate (unrealistic) bending waves as the simulation proceeds.

The main characteristics of the forward cast will be presently discussed for a benchmark cast. Then, we will highlight how this cast is influenced by two sample effects, namely the added drag from an attached fly, and the shape of the rod tip path.

4.1. CHARACTERISTICS OF THE FORWARD CAST

Figure 7 shows the prediction of a forward cast including the formation and propagation of the loop for eight selected times. The loop is initiated at the abrupt "stop" of the rod tip and then freely propagates to the left under the action of air drag and line tension, bending and weight.

A fundamental understanding of the loop formation and propagation process can be gained by studying Figures 8 and 9 which illustrate the velocity components and tension at the extreme ends of the fly line. Note that the velocity components shown in Figure 8 for the rod tip end of fly line define boundary conditions (36) and (37) for an approximate rod tip motion. Three distinct phases of fly line response can be clearly identified in these figures.

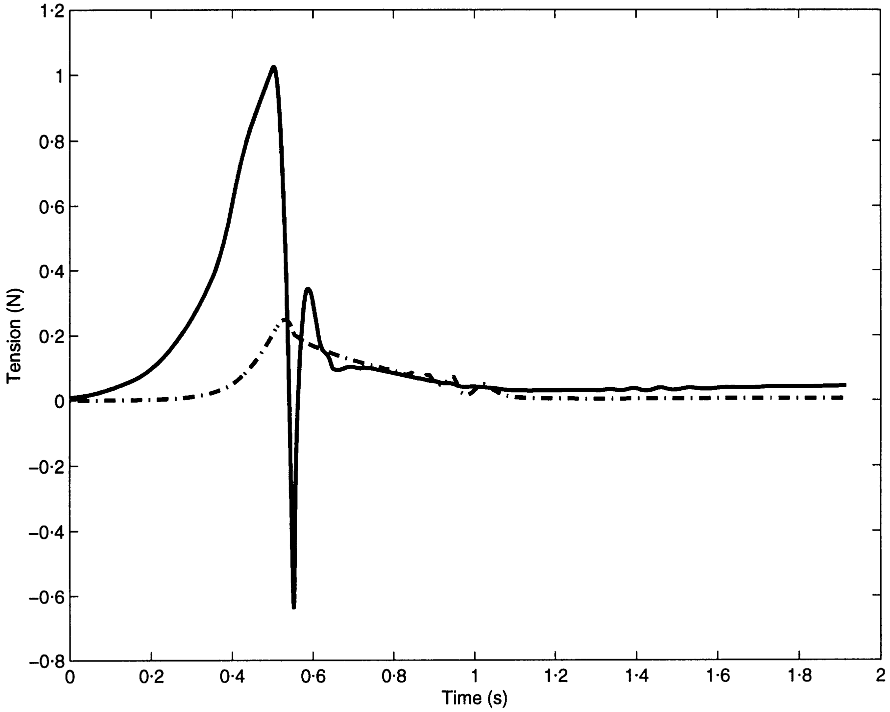

Figure 9. Time history of the fly line tension at the extreme ends of the fly line: ——, rod tip end of the fly line; ·-·-·-, fly end of the fly line.

The first phase, from $t = 0$ s to approximately $t = 0{\cdot}5$ s is characterized by a nearly straight-line motion of the fly line as it accelerates from rest in the back cast. From Figure 8, note that the vertical velocities of the extreme ends of the fly line are nearly zero during this time interval, and that the horizontal velocities are nearly identical and increase smoothly and rapidly from zero to approximatively 30 m/s at the conclusion of this phase. Simultaneously, appreciable tension develops at the rod tip end of the fly line and to a lesser degree at the fly end of the fly line as depicted in Figure 9. Thus, during this first phase, the fly line behaves essentially like a rigid body accelerated horizontally at the rod tip. The second phase, which lasts from approximately $t = 0{\cdot}5$ to 0·7 s corresponds to the abrupt deceleration of the rod tip as it dips slightly below the horizontal. Large velocity differentials are now created between the extreme ends of the fly line as shown in Figure 8. In particular, the rod tip end of the fly line is brought to rest while the fly end continues to move horizontally with appreciable speed while simultaneously falling with modest speed. During this phase, the tension in the fly line at the rod tip drops significantly (becoming compression), while the tension at the fly end is slightly reduced. The large velocity differences at the extreme ends and the sharp drop in line tension at the rod tip are key elements in loop formation. The remainder of the cast beyond $t = 0{\cdot}7$ s defines the third phase during which the loop propagates freely to the left while slowly falling under the action of gravity. During this phase, the horizontal velocities of the extreme ends decrease as energy is dissipated by air drag. The vertical velocity for the fly end achieves a maximum at the turnover of the loop at about $t = 1$ s, as expected.

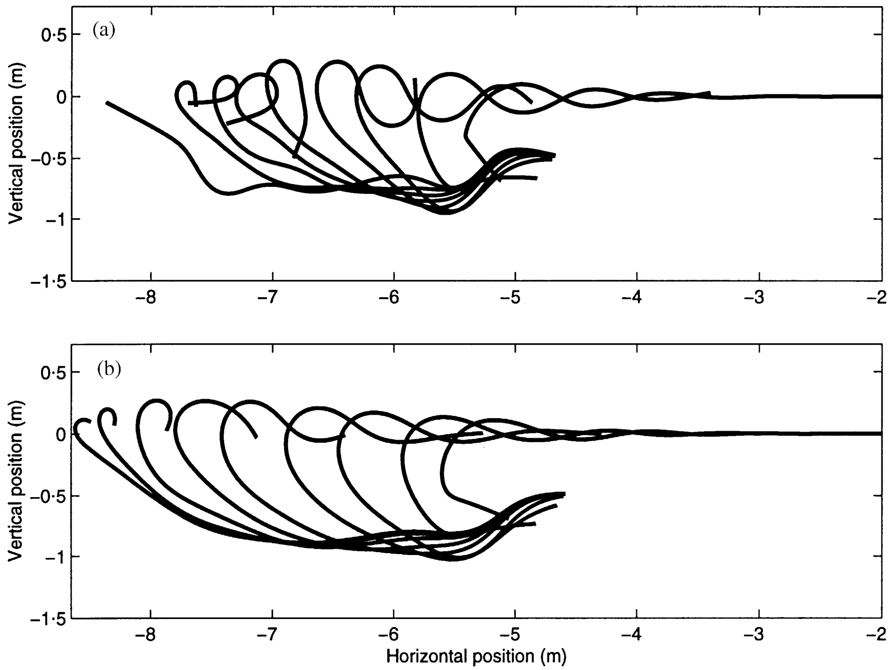

Figure 10. Influence of fly drag: (a) numerical calculation of a cast without a fly; (b) numerical calculation of same cast with a fly.

4.2. INFLUENCE OF THE FLY DRAG

The cast above includes the effect of a medium (size 12) dry fly with the assumed mass, drag, and radius (characteristic dimension) reported in Table 2. At first glance, one might be tempted to ignore the influence of an attached fly altogether. However, fly casters have long observed that the additional weight and drag produced by an attached fly can materially alter a cast. This observation is confirmed by the results illustrated in Figure 10.

Figure 10(a) illustrates a cast computed without the fly while Figure 10(b) shows the very same cast with the fly. All other parameters for these two casts are identical, and gravity is ignored in both so that conclusions can be drawn specifically about the role of added fly drag. Inspection of these two results reveals a significant role played by fly drag during loop propagation and final loop turnover (the “third phase” described above). Without a fly, the loop in Figure 10(a) ultimately collapses upon itself and would likely tangle. By contrast, with a fly, the loop in Figure 10(b) propagates smoothly (and realistically) to the left where it finally turns over at the conclusion of the forward cast.

Figure 11 shows the time histories of the velocity components for the fly end of the fly line for the same two casts, while Figure 12 shows the corresponding fly line tension at the rod tip end. Note from Figure 11 that, without a fly, oscillations appear in the vertical and horizontal velocity components. These oscillations describe the significant whipping motion of the (bare) end of the fly line during the final stages of loop propagation and turnover that would likely result in tangling. By contrast, with a fly, these velocity components vary rather smoothly with time. Equally important, observe from Figure 12 that the peak fly line tension at the rod tip end increases by approximately 25% upon the

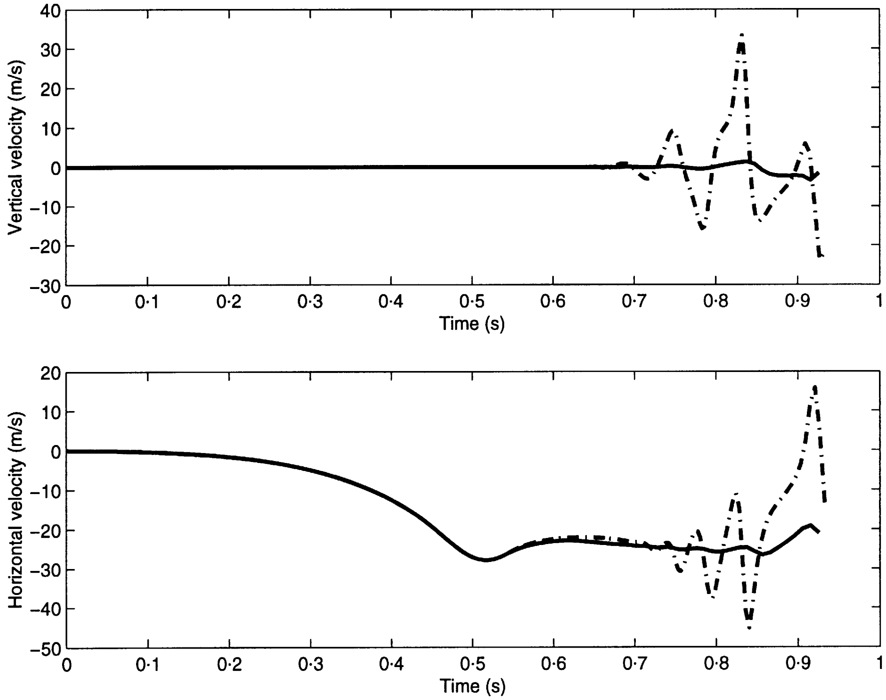

Figure 11. Time history of the velocity components at the fly end of the fly line with and without fly: ·-·-·-, cast without fly; ——, same cast with an attached fly.

addition of a fly. This tension peak occurs at the conclusion of the "first phase" and the increase here derives from the added (significant) drag force of the fly that serves to further tension the fly line during this phase of casting.

4.3. INFLUENCE OF THE ROD TIP PATH

Arguably the greatest factors influencing fly casting are those that control the path followed by the tip of the fly rod. The shape of this path, as well as the speed along it, are the means by which a fly caster controls the motion of the fly line. Consequently, much attention in fly casting instruction concentrates on the rod tip path; see, for example, [1, 2].

The significance of the rod tip path in fly casting dynamics is captured in boundary conditions (36) and (37) which define the velocity components of the rod tip. These boundary conditions are also the most challenging quantities to specify in this model of fly line dynamics as the authors remain unaware of any published data for the velocity of the rod tip. As a start, we have analyzed video images of fly casting featured in reference [16] and have estimated both the shape of a typical path as well as the speed along it. We now describe how reasonably small changes to this estimated path can materially alter the resulting loop. Figure 13 illustrates two assumed rod tip paths. Each begins with a straight horizontal trajectory that ends with a stop below the horizontal. For the path denoted as #1, the "dip" below the horizontal is nearly linear while for the path denoted as #2, the "dip" is rounded. The differences in the shape of these paths are responsible for the

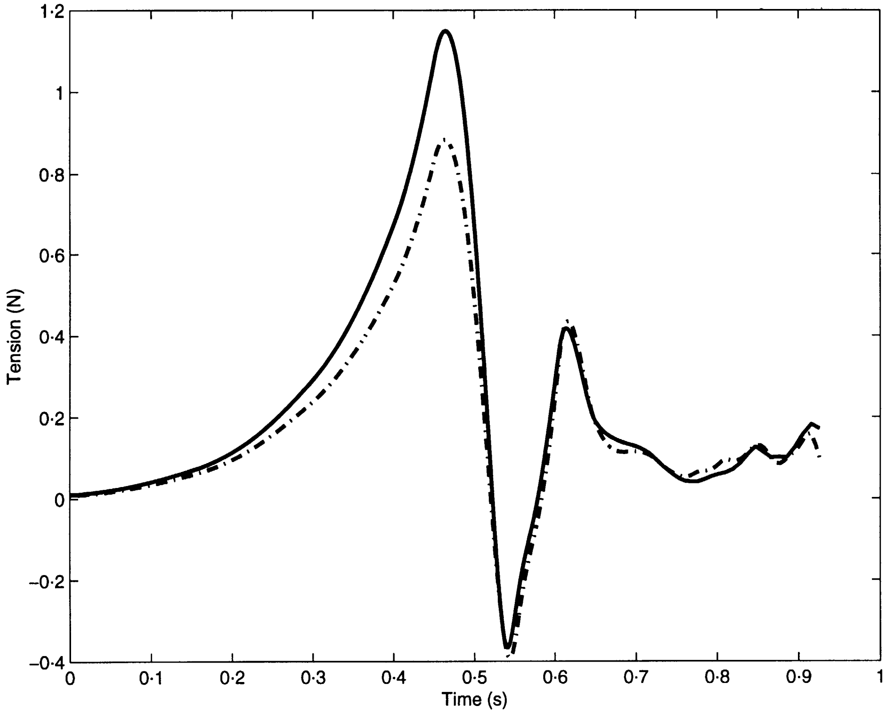

Figure 12. Time history of the tension at the rod tip with and without an attached fly: ·-·-·-, cast without fly; ——, same cast with an attached fly.

markedly different loop shapes shown in Figure 14. Path #1 produces the loop shown in Figure 14(a) that has a leading edge with a positive slope and with the greatest curvature near the bottom. By contrast, path #2 produces the loop shown in Figure 14(b) with a leading edge having a negative slope and with the greatest curvature near the top. This particular loop, sometimes referred to as a *climbing loop*, is often very desirable and may be a hallmark of an expert caster. The two paths also lead to two qualitatively distinct tensions in the fly line as shown in Figure 15. Note that for path #1, the fly line (at the rod tip) experiences compression during two time intervals as opposed to the single time interval for path #2. These two compression intervals are responsible for the two "lobes" that appear in the loop for path #1; refer Figure 14(a).

5. SUMMARY AND CONCLUSION

This paper establishes a continuum model for fly line dynamics and a requisite numerical algorithm to simulate fly casting. A planar elastica is introduced to model the large, non-linear dynamic deformations of the fly line when forming a propagating loop. The model, which readily incorporates the taper of the fly line, captures the effects of fly line tension, drag, self-weight, and bending. The associated boundary conditions capture the effects of the imposed motion at the tip of the fly rod at one end of the fly and the forces acting upon the attached fly at the other end. The numerical algorithm is based upon that in [12, 14] with improvements that address the rapid rotations and accelerations experienced by the fly line during loop formation and propagation.

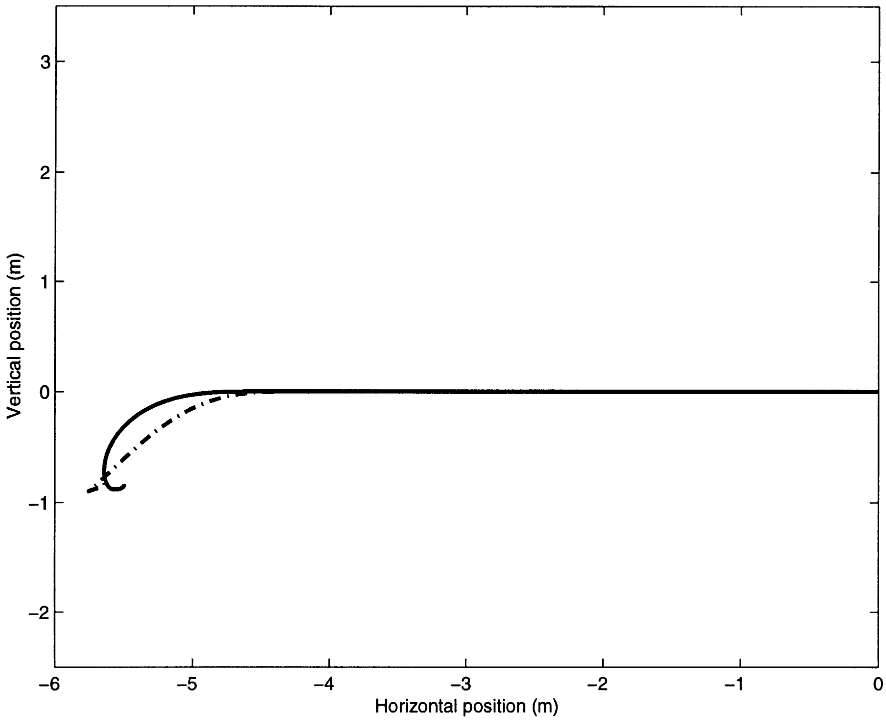

Figure 13. Two example paths for the rod tip: ······, path #1; ——, path #2.

The model and numerical algorithm are employed to study the forward cast during standard overhead casting. The initial conditions describe a perfectly laid out back cast from which the forward cast is initiated. Inspection of simulated results reveals three distinct phases of fly line response during the forward cast. These include the nearly rigid-body acceleration of the fly line from the back cast, the formation of a loop following the abrupt stop of the rod tip, and the propagation and eventual turnover of the loop. The first phase is characterized by very rapid but smooth increases in fly line tension and speed with little to no flexible-body deformation of the fly line. The abrupt stop of the rod tip initiates the second phase that is characterized by a dramatic drop in the tension and speed of the fly line at the rod tip. The resulting velocity difference between the extreme ends of the fly line generates rapid rotations (flexible-body deformation) of the line during the creation of a loop. During the third phase, this loop propagates along the fly line under the influence of line tension and air drag while falling slightly under the influence of gravity.

The model is further exercised to understand the influence of two sample effects on fly casting, namely the drag created by the attached fly and the shape of the path of the rod tip. The drag created by the attached fly servers to further tension the fly line during the first phase of the forward cast and to maintain tension and to dissipate fly line oscillations during the third phase, and particularly during the critical loop turnover. The shape of the path described by the rod tip substantially controls the shape of the resulting loop, an observation well known to casting experts. The examples presented herein reinforce this conclusion by illustrating two qualitatively different loops that form as a result of an arguably modest change to the rod tip path. This sensitivity underscores the sheer amount of practice required to develop highly skilled casting techniques [1, 2].

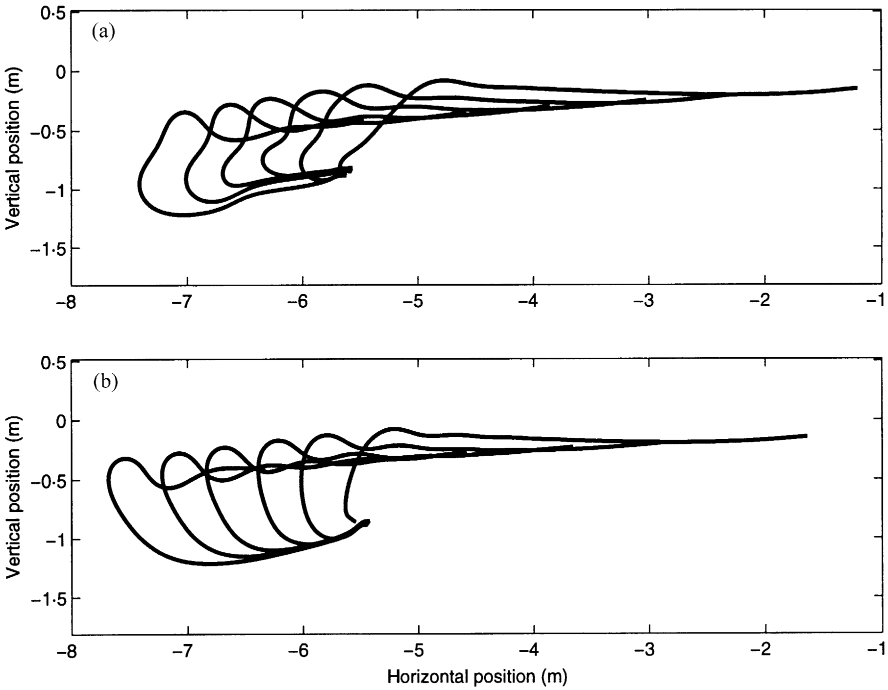

Figure 14. Influence of rod tip path: (a) numerical calculation of cast using path #1; (b) numerical calculation of cast using path #2.

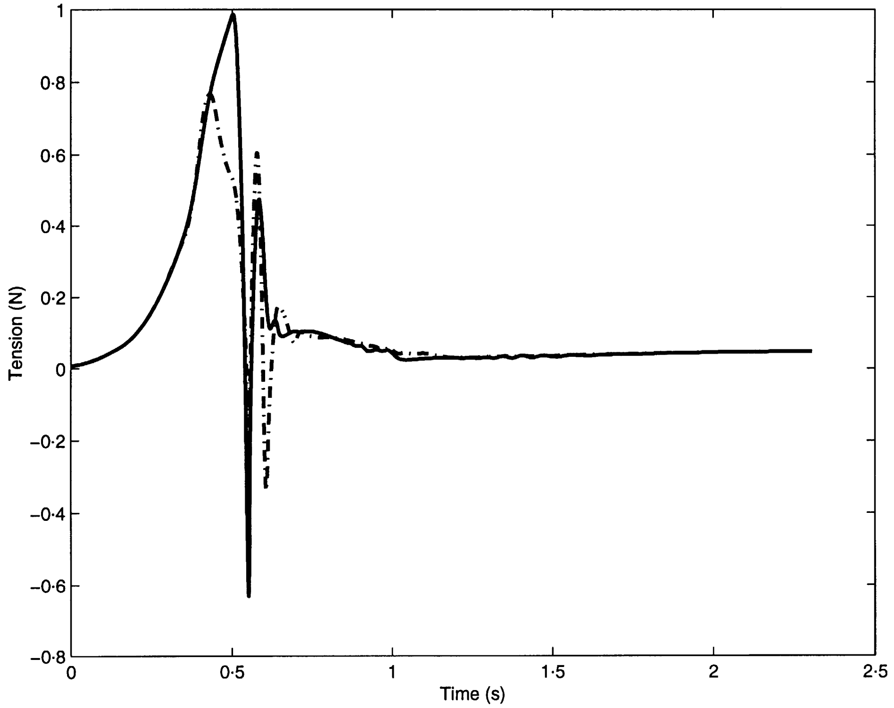

Figure 15. Time history of the fly line tension at the rod tip end: ·-·-·-, for path #1; ——, for path #2.

The objective of this paper is to establish a mathematical model and numerical algorithm for simulating the dynamics of fly casting. This objective is aligned with the goal of fostering innovations in fly casting equipment design and in fly casting technique and instruction using computer-based simulation [3]. The sample results presented here are limited, but they are also representative of numerous other studies that could be conducted to support this goal.

ACKNOWLEDGMENTS

The authors wish to acknowledge the supplies and many technical discussions offered by Mr. Bruce Richards of Scientific Anglers and the Rackham Predoctoral Fellowship offered by the Horace H. Rackham School of Graduate Studies at the University of Michigan.

REFERENCES

1. M. K. KRIEGER 1987 *The Essence of Flycasting*. San Francisco, CA: Club Pacific.
2. B. KREH 1991 *Modern Fly Casting Method*. Birmingham, AL: Odysseus Editions.
3. D. PHILLIPS 2000 *The Technology of Fly Rods*. Portland, OR: Frank Amato Publications, Inc.
4. G. A. SPOLEK *http://www.me.pdx.edu/graig/cast-ref.htm*.
5. G. A. SPOLEK 1986 *American Journal of Physics* **54**, 832–835. The mechanics of flycasting: the fly line.
6. S. LINGARD 1988 *American Journal of Physics* **56**, 756–757. Note on the aerodynamics of a fly line.
7. J. M. ROBSON 1990 *American Journal of Physics* **58**, 234–240. The physics of flycasting.
8. C. S. GATTI and N. C. PERKINS 2001 *ASME Bioengineering Conference*, BED-Vol. 50, *Snowbird, UT*, 277–278. Numerical analysis of flycasting mechanics.
9. M. S. TRIANTAFYLLOU and C. T. HOWELL 1994 *Journal of Sound and Vibration* **173**, 443–447. Dynamic response of cables under negative-tension: an ill-posed problem.
10. C. T. HOWELL 1992 *International Journal of Offshore and Polar Engineering* **2**, 110–113. Numerical analysis of 2-D nonlinear cable equations with applications to low-tension problems.
11. J. J. BURGESS 1993 *International Journal of Offshore and Polar Engineering* **3**, 197–204. Bending stiffness in a simulation of undersea cable deployment.
12. Y. SUN 1996 *Ph.D. Dissertation, University of Connecticut*. Modeling and Simulation of Low-tension Oceanic Cable/Body Deployment.
13. D. T. GREENWOOD 1988 *Principles of Dynamics*. Englewood Cliffs, NJ: Prentice-Hall, second edition.
14. Y. SUN 1992 *Masters Thesis, Oregon State University*. Nonlinear Response of Cable/Lumped-body System by Direct Integration Method with Suppression.
15. J. W. LEONARD 1968 *American Society of Civil Engineers Journal of Structure and Division* **99**, 2861–2883. Dynamic response of initially-stressed membrane shells.
16. M. KRIEGER 1985 *The Essence of Flycasting*, video produced by Club Pacific.

APPENDIX A: DETAILS OF SUPPRESSION METHOD

Let

$$\{\mathbf{h}^o\} = [y_p^3(s,\hat{t})y_p^5(s,\hat{t})y_p^6(s,\hat{t})]^{\mathrm{T}}, \quad [\mathbf{H}] = [\mathbf{y}_h^3(s,\hat{t})\mathbf{y}_h^5(s,\hat{t})\mathbf{y}_h^6(s,\hat{t})]^{\mathrm{T}} \qquad \text{(A.1, A.2)}$$

denote the components of the particular and homogeneous solutions that are monitored for suppression. In particular, $y_p^i(s,\hat{t})$ indicates the ith component of the vector $\mathbf{y}_p(s,\hat{t})$ and $\mathbf{y}_h^i(s,\hat{t})$ represents the 3×1 vector that is obtained by taking the ith row of the matrix $\mathbf{y}_h(s,\hat{t})$.

Let $\{\mathbf{h}^k\}$, $k = 1, 2, 3$ be the columns of the matrix $[\mathbf{H}]$. The solutions $\{\mathbf{h}^k\}$, $k = 0, 1, 2, 3$ are suppressed at the suppression points by comparing their values to prescribed limits:

$$\{\mathbf{p}^o\} = \begin{Bmatrix} p_{10} \\ p_{20} \\ p_{30} \end{Bmatrix}, \quad \{\mathbf{p}^1\} = \begin{Bmatrix} p_{11} \\ 0 \\ 0 \end{Bmatrix}, \quad \{\mathbf{p}^2\} = \begin{Bmatrix} 0 \\ p_{22} \\ 0 \end{Bmatrix}, \quad \{\mathbf{p}^3\} = \begin{Bmatrix} 0 \\ 0 \\ p_{33} \end{Bmatrix}. \tag{A.3}$$

These limits are satisfied by imposing

$$[\mathbf{H}]\{\boldsymbol{\zeta}^k\} + \{\mathbf{h}^k\} = \{\mathbf{p}^k\}, \quad k = 0, 1, 2, 3, \tag{A.4}$$

where $\{\boldsymbol{\zeta}^k\}$ contains the suppression coefficients for the kth solution.

Solving for the suppression coefficients yields

$$\{\boldsymbol{\zeta}^k\} = [\mathbf{H}]^{-1}(\{\mathbf{p}^k\} - \{\mathbf{h}^k\}), \quad k = 0, 1, 2, 3, \tag{A.5}$$

from which the recombined, suppressed particular and homogeneous solutions are formed as

$$\mathbf{y}_{ps}(s, \hat{t}) = \mathbf{y}_p(s, \hat{t}) + \mathbf{y}_h(s, \hat{t})\boldsymbol{\zeta}^o, \tag{A.6}$$

$$\mathbf{y}^i_{hs}(s, \hat{t}) = \mathbf{y}^i_h(s, \hat{t}) + \mathbf{y}_h(s, \hat{t})\boldsymbol{\zeta}^i, \quad i = 1, 2, 3, \tag{A.7}$$

where $\mathbf{y}_{ps}(s, \hat{t})$ is the new particular solution obtained after suppression, $\mathbf{y}_p(s, \hat{t})$ is the particular solution before suppression, $\mathbf{y}_h(s, \hat{t})$ is the matrix containing the homogeneous solutions, $\boldsymbol{\zeta}^o$ is the suppression coefficient for the suppression of the particular solution, $\mathbf{y}^i_{hs}(s, \hat{t})$ is the ith homogeneous solution obtained after suppression, and $\boldsymbol{\zeta}^i$ is the suppression coefficient for the suppression of the homogeneous solution.